Journal of Catalysis 272 (2010) 109–120

Contents lists available at ScienceDirect

Journal of Catalysis

journal homepage: www.elsevier.com/locate/jcat

The total oxidation of propane over supported Cu and Ce oxides: A comparison of single and binary metal oxides

Philippe M. Heynderickx [a], Joris W. Thybaut [a,*], Hilde Poelman [a], Dirk Poelman [b], Guy B. Marin [a]

[a] Laboratory for Chemical Technology, Department of Chemical Engineering, Ghent University, Krijgslaan 281 (S5), Ghent B-9000, Belgium
[b] Department of Solid State Sciences, LumiLab, Ghent University, Krijgslaan 281 (S1), Ghent B-9000, Belgium

ARTICLE INFO

Article history:
Received 21 December 2009
Revised 2 March 2010
Accepted 5 March 2010
Available online 20 April 2010

Keywords:
Copper
Ceria
Total oxidation
Propane
Synergy
Turnover frequency

ABSTRACT

The total oxidation of propane is studied by means of steady-state experiments over a set of Cu- and Ce-based catalysts at a propane inlet partial pressure of 0.6 kPa, an oxygen partial pressure of 3.5 kPa and temperatures from 595 to 648 K. The catalysts were characterized by inductively coupled plasma (ICP), Brunauer–Emmett–Teller specific surface area (BET), temperature-programmed desorption (TPD), X-ray diffraction (XRD), pulse reduction–reoxidation, and H_2- and C_3H_8-temperature-programmed reduction (TPR). A synergistic effect between cupric oxide, CuO, and ceria, CeO_2, is observed using a Mars–van Krevelen model to describe the kinetic data: the activation energies for reduction and reoxidation, obtained on the binary metal oxide catalyst with both cupric oxide and ceria, are 20 kJ mol^{-1} lower than those obtained on the single Cu- or Ce-based catalysts. The corresponding turnover frequencies are the highest.

1. Introduction

Nowadays, hydrocarbon emissions from both stationary and non-stationary sources are subjected to strict legislation. Catalytic oxidation offers the advantage that volatile organic component (VOC) can be removed from effluent streams with low VOC concentration at relative low temperatures [1]. Metal oxide catalysts offer a range of technical and commercial advantages that make them a viable alternative to noble metals. Long lifetime, poisoning and masking tolerance, capability of regeneration, availability in a large variety of metal oxide compositions, shapes and sizes, and low price lay the foundation for successful applications [2].

Cupric oxide is known to give highly active catalysts in total oxidation reactions [3–5]. The catalytic properties of the supported cupric oxide-based catalysts are enhanced by the addition of ceria [6,7]. The effect of the preparation method of Cu- and Ce-based catalytic systems on the activity has been intensively studied [8,9]. Nevertheless, up to now, no systematic investigation including catalytic activity and kinetics has been performed. The present paper applies inductively coupled plasma (ICP), Brunauer–Emmett–Teller specific surface area (BET), temperature-programmed desorption (TPD) and X-ray diffraction (XRD) in order to characterize three Cu- and Ce-based catalysts, prepared by the wet impregnation technique. Next to these physical characterizations, pulse reduction–reoxidation experiments, H_2- and C_3H_8-temperature-programmed reduction (TPR) experiments and catalytic steady-state experiments in propane total oxidation are performed to relate physical, catalytic and kinetic properties.

2. Procedures

2.1. Catalysts

Three commercial catalysts are used, see Table 1: a CuO–CeO_2/γ-Al_2O_3 catalyst synthesized by impregnation [10,11] with precursors $Cu(NO_3)_2$ and $Ce(NO_3)_4$ on a γ-Al_2O_3 support, denoted as Cu-CeO. Catalyst CuO is obtained by impregnation of θ-Al_2O_3 with $Cu(NO_3)_2$. Further, a catalyst with pure ceria, denoted as CeO, is obtained by impregnation of a γ-Al_2O_3 support, with a lower surface area than the latter, with $Ce(NO_3)_4$.

2.2. Catalyst characterization

The bulk chemical composition of the tested catalysts was determined by means of inductively coupled plasma atomic emission spectrometry (ICP-AES) (IRIS Advantage system, Thermo Jarrell Ash). N_2 physisorption at 77 K is applied to determine the BET specific surface area using a Gemini V (Micromeritics) automated system. BET values with their 95% confidence intervals were obtained by regression of the experimental data in the range $0.05 < p/p^0 < 0.30$ with the linear BET equation [12]. The catalyst's

* Corresponding author. Fax: +32 (0) 9 264 49 99.
E-mail address: Joris.Thybaut@UGent.be (J.W. Thybaut).

0021-9517/$ - see front matter © 2010 Elsevier Inc. All rights reserved.
doi:10.1016/j.jcat.2010.03.006

Nomenclature

Roman symbols

$a_{\beta^*,i}$	constant in Eq. (1) (mol s^{-1})
A	constant in Eq. (5) ($mol_{C_3H_8}$ $mol^{-1}_{C_3H_8,0}$)
A	preexponential factor, used in Eq. (2) (s^{-1})
A_i	surface area of the peak of component i (V s)
B	constant in Eq. (5) ($mol_{C_3H_8,0}$ $kg^{-1}_{cat} s^{-1}$)
C_i	concentration of adsorbed moles for component i (mol_i kg^{-1}_{cat})
C_O	oxygen storage capacity (mol_O kg^{-1}_{cat})
C_t	total concentration of active sites (mol kg^{-1}_{cat})
d_i	calibration factor for component i (V s mol^{-1})
D	dispersion (mol mol^{-1})
E	activation energy (kJ mol^{-1})
F_i	molar flow of component i (mol_i s^{-1})
h	Planck constant (J s)
$k_{app,0}$	initial apparent rate coefficient, see Eq. (7) ($mol_{C_3H_8}$ kg^{-1}_{cat} s^{-1} $kPa^{-n_{C_3H_8}-n_{O_2}}$)
k_B	Boltzmann constant (J K^{-1})
$k_{C_3H_8}$	reduction rate coefficient, see Eq. (S-13) ($mol_{C_3H_8}$ kg^{-1}_{cat} kPa^{-1})
k_{O_2}	reoxidation rate coefficient, see Eq. (S-14) (mol_{O_2} kg^{-1}_{cat} s^{-1} kPa^{-1})
K	shape factor, used in Eqs. (S-2) and (S-4) (–)
L	average particle size (nm)
M	molar mass (kg mol^{-1})
n	reaction order (–)
n_i	number of carbon atoms in component i (–)
Δn	change in number of moles (–)
N_C	number of carbon containing components (–)
p	partial pressure (kPa)
N_P	number of peaks in a TPR experiment (–)
r	specific reaction rate ($mol_{C_3H_8}$ kg^{-1}_{cat} s^{-1})
r_{col}	collision rate (mol $m^{-1}_{cat} s^{-1}$)
R	universal gas constant (kJ mol^{-1} K^{-1})
s	sticking probability (–)
$\Delta^{\neq}S^0$	standard activation entropy (J mol^{-1} K^{-1})
$\Delta_r S^0$	standard reaction entropy (J mol^{-1} K^{-1})
S_0	initial molar amount of reducible substance (mol)
T	temperature (K)
TOF_0	initial turnover frequency ($mol_{C_3H_8}$ mol^{-1}_O s^{-1})
W_{cat}	catalyst mass (kg_{cat})
$X_{C_3H_8}$	propane conversion ($mol_{C_3H_8}$ $mol^{-1}_{C_3H_8,0}$)
y	mass percentage (kg kg^{-1})

Greek symbols

α_s	BET specific surface area (m^2_{cat} g^{-1}_{cat})
β	half-peak width, used in Eqs. (S-2) to (S-4) (–)
β^*	heating rate (K s^{-1})
ε	lattice distortion parameter (mm m^{-1})
ε	porosity (m^3 m^{-3})
θ	diffraction angle, used in Eqs. (S-2) to (S-4) (rad)
θ	fraction of active sites (–)
λ	X-ray wavelength (m)
Λ	TCD outlet signal, corrected for blank experiment (mol s^{-1})
ρ	density (kg m^{-3})
σ	standard deviation (dep.)
Ω	cross-section (m^2)

Subscripts

app	apparent
b	bed
cat	catalyst
i	component i
O^*	oxidized site
p	particle
0	initial, inlet
$*$	reduced site

Superscripts

0	standard
$*$	lumped
–	average
$\neq$	transition state

Abbreviations and acronyms

BET	Brunauer, Emmett and Teller
ICP	inductively coupled plasma
MVK	Mars-van Krevelen
OSC	oxygen storage capacity
TCD	thermal conductivity detector
TOF	turnover frequency
TPD	temperature-programmed desorption
TPR	temperature-programmed reduction
VOC	volatile organic component
XRD	X-ray diffraction

oxygen storage capacity (OSC), C_O, is determined by pulse chemisorption experiments using a Micromeritics AutoChem 2920. Temperature-programmed desorption (TPD) analysis has been performed in a Micromeritics AutoChem 2920. Sorptive molecules are carbon dioxide, carbon monoxide and oxygen. Carbon dioxide was used to measure the basicity of the catalysts. Propane and oxygen are used as probe because they are reactants [13].

Crystallographic analyses for the tested catalysts were performed by means of X-ray diffraction (XRD) measurements in θ–2θ mode using a Bruker-AXS D8 Discover apparatus with lynx eye detector covering 3° and 192 channels over the range 15–85° with a step of 0.04°. For evaluations of the average particle size, (L), and the lattice distortion, (ε), the Scherrer equation [14] and the Williamson–Hall equation [15] were applied on XRD experimental data, with correction for the instrumental width using a LaB_6 measurement. Next to the three catalysts, as received, structural characterization on six additionally treated samples is performed: all catalysts are reduced up to 923 K under a flow of 0.05 mol mol^{-1} H_2 in Ar and a total molar flow rate of 4.5×10^{-5} mol s^{-1} at 10 K min^{-1}. CuCeO is additionally reduced up to 623 and 1323 K. Finally, CuCeO is examined, which has been extensively used during 6000 h in propane total oxidation conditions [16]. Table 3 lists all tested catalysts with the corresponding reduction treatment.

Experimental details of the characterization techniques can be found in Supplementary content.

The determination of the particle porosity and the particle density is described in Supplementary content, see Sections S.8 and S.9.

2.3. Temperature-programmed reduction

H_2-TPR experiments are performed at heating rates of 2.5, 5.0, 7.5, 10.0, 15.0, 20.0 and 25.0 K min^{-1} up to 973 K under a flow of 0.05 mol mol^{-1} H_2 in Ar using 100 mg of catalyst material and a total molar flow rate of 4.5×10^{-5} mol s^{-1}. H_2-TPR experiments on the support material are performed at a heating rate of 10 K min^{-1}.

Table 1
Bulk chemical composition, y_M, specific surface area, α_s, the catalyst porosity, ε_p, the catalyst density, ρ_{cat}, and the corresponding average pore radius, $\bar{r}$, for the tested catalysts and the corresponding supports.

	y_M[a] (wt.%)		α_s[b] ($m^2_{cat}\ g^{-1}_{cat}$)	ε_{cat}[c] ($m^3_f\ m^{-3}_{cat}$)	ρ_{cat}[a] ($kg_{cat}\ m^{-3}_{cat}$)	$\bar{r}$[d] (nm)
	Cu	Ce				
Catalyst						
CuCeO	9.2 ± 0.1	5.2 ± 0.1	156.3 ± 0.9	0.62 ± 0.01	3254 ± 3	6.3 ± 0.2
CuO	10.7 ± 0.6	–	80.5 ± 1.0	0.63 ± 0.02	3567 ± 4	12.0 ± 1.3
CeO	–	4.8 ± 0.1	143.4 ± 2.2	0.69 ± 0.02	3183 ± 4	9.5 ± 1.0
Support						
CuCeO	–	–	181.7 ± 2.6	0.60 ± 0.01	2978 ± 9	5.6 ± 0.2
CuO	–	–	85.2 ± 1.4	0.67 ± 0.02	3408 ± 2	14.0 ± 1.0
CeO	–	–	151.9 ± 2.3	0.69 ± 0.01	3100 ± 17	9.4 ± 0.4

[a] Given standard deviations are based on replicate measurements.
[b] Confidence intervals (95%) are reported, obtained by regression of the experimental data in the range $0.05 < p/p^0 < 0.30$ with the linear BET equation [12].
[c] Confidence intervals (95%) are reported, obtained by regression of the experimental data, see Fig. S-1, with Eq. (S-10).
[d] Standard deviations are based on error propagation, using Eq. (S-11).

Table 2
Uptake of carbon dioxide and carbon monoxide in temperature-programmed desorption (TPD) experiments and oxygen storage capacity, C_O, obtained from oxygen pulse chemisorption experiments after maximal reduction with H_2 at 673 K. Calculation of standard deviations can be found elsewhere [19].

	Uptake (mmol kg^{-1}_{cat})		C_O ($mol_O\ kg^{-1}_{cat}$)
	CO_2	CO	
Catalyst			
CuCeO	21.6 ± 1.2	38.7 ± 2.1	1.22 ± 0.06
CuO	14.6 ± 0.8	22.5 ± 1.2	1.37 ± 0.07
CeO	49.8 ± 2.6	0.0[a]	0.07 ± 0.01
Support			
CuCeO	64.7 ± 3.3	0.2 ± 0.1	0.0[a]
CuO	24.1 ± 1.3	0.4 ± 0.1	0.0[a]
CeO	41.5 ± 2.2	0.0[a]	0.0[a]

[a] Not significantly different from zero.

Table 3
Average particles diameter, obtained via XRD analysis and Eq. (S-2). Details of the H_2-TPR pretreatment are given in Section S.5.

Sample number	Catalyst	Average particle diameter (nm)					
		CuO	Cu	CeO_2	γ-Al_2O_3	θ-Al_2O_3	$CeAlO_3$
1	CuCeO[a]	72.2	–	4.4	4.6	–	–
2	CuCeO[b]	–	102.9	5.4	5.3	–	–
3	CuCeO[c]	–	198.7	5.6	5.3	–	–
4	CuCeO[d]	–	52.7	–	6.1	–	40.9
5	CuCeO[e]	49.1	–	7.4	5.0	–	–
6	CuO[a]	34.0	–	–	–	22.9	–
7	CuO[c]	–	79.8	–	–	22.6	–
8	CeO[a]	–	–	8.6	5.4	–	–
9	CeO[c]	–	–	8.6	5.1	–	–
Support							
10	CuCeO[a]	–	–	–	4.1	–	–
11	CuO[a]	–	–	–	–	15.2	–
12	CeO[a]	–	–	–	5.3	–	–

[a] As received.
[b] $T_{max,red}$ = 623 K
[c] $T_{max,red}$ = 923 K
[d] $T_{max,red}$ = 1323 K
[e] After 6000 h of catalytic reaction conditions.

No H_2 consumption is observed in the examined temperature range.

The TCD outlet signal after baseline correction, $\Lambda_{\beta^*}(T)$, corresponding to a heating rate β^*, can be written as a sum of N_P gaussian peaks with average value $T_{\beta^*,i}$ and standard deviation $\sigma_{\beta^*,i}$ for $i = 1, \ldots, N_P$, see Eq. (1). The number of gaussian peaks N_P corresponds to the number of significant observable peaks in the TCD outlet signal.

$$\Lambda_{\beta^*}(T) = \sum_{i=1}^{N_P} a_{\beta*,i} \exp\left[-\frac{(T - T_{\beta*,i})^2}{2\sigma^2_{\beta*,i}}\right] \quad (1)$$

Kinetic parameters of the reduction process, preexponential factor, A_i, and activation energy, E_i, are supplied by the so-called Redhead equation, see Eq. (3), originating from a power law rate expression [17], see Eq. (2), with initial condition for the fraction of oxidized sites $\theta_{O^*} = \theta_{O^*,0} = 1$ at $T = T_0$. For a first-order dependency on the oxygen fractional coverage, n equals unity. This corresponds to the catalyst reduction reaction $H_2 + O^* \rightarrow H_2O + *$. The given approach can be considered as an approximation of more complex kinetic rate expressions for reduction processes and can thus provide a rough estimation of the kinetic parameters in the reduction processes [18]

$$\frac{d\theta_{O^*}}{dT} = A \cdot \exp\left(-\frac{E}{RT}\right) \cdot \frac{\theta^n_{O^*}}{\beta^*} \quad (2)$$

$$\frac{E_i}{RT^2_{\beta^*,i}} = \frac{A_i}{\beta^*_i} \cdot \exp\left(-\frac{E_i}{RT_{\beta^*,i}}\right), \quad i = 1, \ldots, N_P \quad (3)$$

All catalysts are also used in C_3H_8-TPR, performed at 10 K min^{-1} up to 823 K under a flow of 0.05 mol mol^{-1} C_3H_8 in He using 100 mg of catalyst material and a total molar flow rate of 4.5×10^{-5} mol s^{-1}. These reduction experiments will only provide qualitative information.

Experimental details of the temperature-programmed reduction and the used theoretical formulas can be found in Supplementary content, see Section S.7.

2.4. Total oxidation kinetics

Total oxidation of propane experiments at steady-state conditions are performed in a temperature range from 595 to 648 K applying a space time range from 211 to 570 $kg_{cat}\ s\ mol^{-1}_{C_3H_8,0}$ at $p_{C_3H_8,0} = 0.6$ kPa and $p_{O_2,0} = 3.5$ kPa and atmospheric total pressure. Propane conversion values up to 0.73 $mol_{C_3H_8}\ mol^{-1}_{C_3H_8,0}$ are obtained. Details of the propane conversion calculation can be found in Supplementary content, see Section S.10. Blank experiments, performed at the most severe conditions, exhibit no propane conversion [16]. Stability of the catalysts is tested by replicate experiments. Deviations of the observed propane conversion were smaller than 5%. Details of the experimental set-up and procedure are given elsewhere [19].

Based on correlations, given in literature [20], it was verified that concentration and temperature gradients on pellet and reactor scale can be neglected and that a plug-flow regime is established. The steady-state continuity equation for propane is given by

Eq. (4) with the initial condition that $X_{C_3H_8} = 0\ mol_{C_3H_8}\ mol^{-1}_{C_3H_8,0}$ for $\frac{W_{cat}}{F_{C_3H_8,0}} = 0\ kg_{cat}\ s\ mol^{-1}_{C_3H_8,0}$:

$$\frac{dX_{C_3H_8}}{d\left(\frac{W_{cat}}{F_{C_3H_8,0}}\right)} = r \tag{4}$$

The steady-state experimental data are modeled by means of a simple power law rate model and a more sophisticated mechanistic Mars–van Krevelen (MVK) model, from which apparent activation energies for the total oxidation of propane as well as activation energies and preexponential factors for the reduction and reoxidation steps are obtained.

2.4.1. Kinetic models

Experimental propane conversion versus space time curves are fitted with Eq. (5):

$$X_{C_3H_8} = A \cdot \left(1 - \exp\left(-B \cdot \frac{W_{cat}}{F_{C_3H_8,0}}\right)\right) \tag{5}$$

Application of Eqs. (4) and (5) for a zero space time gives an initial specific reaction rate, expressed in $mol_{C_3H_8}\ kg^{-1}_{cat}\ s^{-1}$. Initial turnover frequencies, TOF_0, given in Eq. (6), are obtained when the specific reaction rate is related to the concentration of active sites, which is assumed to be equal to the OSC [19]. This choice is justified in Section 3.7.

$$TOF_0 = \frac{A \cdot B}{C_O} \tag{6}$$

The experimental TOF_0 can be fitted by a power law model, see Eq. (7). When the inlet partial pressure dependencies for the tested catalysts are lumped into one apparent preexponential factor, $k^*_{app,0} = k_{app,0} p^{n_{C_3H_8}}_{C_3H_8,0} p^{n_{O_2}}_{O_2,0}$, an experimental apparent activation energy, E^{obs}_{app}, can be determined from the logarithm of the TOF_0, given in Eq. (6), versus the inverse of the reaction temperature. The corresponding linear relation is given in Eq. (8)

$$TOF_0 = k_{app,0} \cdot \exp\left(-\frac{E^{obs}_{app}}{RT}\right) \cdot p^{n_{C_3H_8}}_{C_3H_8,0} p^{n_{O_2}}_{O_2,0} \tag{7}$$

$$\ln(TOF_0) = \ln k^*_{app,0} - \frac{E^{obs}_{app}}{RT} \tag{8}$$

Another approach is to regress the experimental data by a MVK model, using Eq. (9). This MVK model has been successfully applied in total oxidation reactions over metal oxide catalysts [19,21–25]. It corresponds to a reduction step in which propane reacts with a single oxidized site and with a reoxidation step by gas phase oxygen, involving a single reduced site. The reduction reaction and the reoxidation reaction, adjusted for the stoichiometry of the overall reaction, are equal in the steady-state, and the factor '5' in the denominator of the corresponding rate equation, Eq. (9), originates from the number of oxygen molecules needed in the total oxidation of one propane molecule [26]. Details of the non-isothermal parameter estimation procedure can be found elsewhere [16].

$$r = \frac{k_{O_2} k_{C_3H_8} p_{O_2} p_{C_3H_8}}{k_{O_2} p_{O_2} + 5 k_{C_3H_8} p_{C_3H_8}} \tag{9}$$

The fraction of oxidized sites, θ_{O^*}, is given by Eq. (10). Details on the calculation are given in Section S.11

$$\theta_{O^*} = \frac{k_{O_2} p_{O_2}}{k_{O_2} p_{O_2} + 5 k_{C_3H_8} p_{C_3H_8}} \tag{10}$$

2.4.2. Average fraction of oxidized sites

A theoretical apparent activation energy, E^{calc}_{app}, can be calculated according to Eq. (11) [27]:

$$E^{calc}_{app} = RT^2 \left(\frac{\partial \ln r}{\partial T}\right)_{\underline{p}} \tag{11}$$

A relation between this apparent activation energy and the activation energies for reoxidation, E_{O_2}, and reduction, $E_{C_3H_8}$, can be determined by substitution of the MVK rate expression, see Eq. (9), into Eq. (11). This results in a barycentric combination of the activation energies for oxidation and reduction, see Eq. (12). Details of the calculation are given in Appendix A. The calculated apparent activation energy depends on local conditions, i.e., temperature and partial pressures, see Eqs. (S-18) and (S-19).

$$E^{calc}_{app} = \theta_{O^*} E_{C_3H_8} + (1 - \theta_{O^*}) E_{O_2} \tag{12}$$

An average fraction of oxidized sites for a set of experimental conditions, $\bar{\theta}_{O^*}$, can be obtained from Eq. (13), using Eq. (10):

$$\bar{\theta}_{O^*} = \frac{1}{n} \sum_{i=1}^{n} \theta_{O^*}|_i \tag{13}$$

2.4.3. Standard activation entropy

From the preexponential factors for oxidation and reduction determined in the MVK model, see Eq. (9), the standard activation entropy $\Delta^{\neq}S^0$ for propane and oxygen is obtained using Eq. (14). The right-hand side originates from transition state theory [28] and is corrected for the concentration of active sites, C_t [29]:

$$k_{i,0} = C_t \exp(1 - \Delta n^{\neq}_i)\left(\frac{k_B T^*}{h}\right) \exp\left(\frac{\Delta^{\neq} S^0_i}{R}\right) \tag{14}$$

$\Delta n^{\neq}$ is the change in the number of moles when the activated complex is formed from the reactant(s). For propane and oxygen $\Delta n^{\neq} = -1$ holds. A number-averaged temperature $T = 621$ K is used. When the oxygen storage capacity C_O, see Section 3.7, is used as concentration of active sites, C_t, the activation entropy $\Delta^{\neq}S^0$ can be determined. A more negative value for the activation entropy corresponds to a transition state which is more rigidly bound.

2.4.4. Assessment of parameter estimates

Fu et al. [30] report standard activation entropies for propane C–H bond activation in selective oxidation over molybdenum oxides at 688 K ranging from −100 to −159 J mol^{-1} K^{-1}. Standard reaction entropies at 688 K, $\Delta_r S^0$, for total oxidation, i.e., giving carbon dioxide and water, and partial oxidation of propane toward propene and water are theoretically calculated with B3LYP/6-31 G* as −114 and −87 J mol^{-1} K^{-1} [31]. The latter value has to do with the C–H cleavage in the partial oxidation reaction, whereas total oxidation requires a C–C cleavage, giving rise to a higher entropy gain. Hence, standard activation entropies for total oxidation of propane at 688 K are expected from −130 to −210 J mol^{-1} K^{-1}.

From kinetic gas theory, the rate of collisions, r_{col}, between gas phase molecules i and unit surface area per unit time is given by Eq. (15):

$$r_{col,i} = \frac{p_i}{\sqrt{2\pi M_i RT^*}} \tag{15}$$

Since not all of these collisions result in chemisorption, needed for reaction on the catalyst surface, the sticking probability, s, for oxygen and propane is defined as the ratio of adsorption rate of oxygen, see Eq. (S-13), and propane, see Eq. (S-14), and the theoretical collision rate of the corresponding molecules, see Eq. (15) [26]. This probability gives the fraction of collisions that do lead to chemisorption, followed by catalytic reaction.

The estimated activation energies for the total oxidation of propane, E^{obs}_{app}, obtained by TOF_0 analysis, and $E_{C_3H_8}$ and E_{O_2}, obtained by regression of the MVK model, see Eq. (9), are compared with liter-

ature values reported for the same reaction over metal oxide catalysts. Typical values for the activation energies in propane combustion reactions over oxide catalysts range from 70 to 110 kJ mol^{-1} [32].

3. Catalyst characterization

3.1. Bulk chemical composition

The bulk chemical composition for the tested catalysts is given in Table 1. The total metal content is almost constant.

3.2. Specific surface area

The BET specific surface areas, α_s, are also given in Table 1. After the preparation of the catalysts, a loss 14% of the initial specific surface area is observed for CuCeO, i.e., the value for the applied support, which is not uncommon after impregnation and a subsequent calcination step in the preparation [33]. For the other catalysts, CuO and CeO, a loss of 6% is observed.

From Table 1, it is observed that the impregnation procedure, see Section 2.1, does not significantly alter the average pore diameter, $\bar{r}$, for CuO and CeO, compared to the supports. A small increase for CuCeO is observed.

3.3. Oxygen storage capacity

Table 2 gives the OSC for the tested catalysts at 673 K. For the supports, no oxygen uptake after reduction with H_2 is observed. Since every catalyst sample is pretreated in air during 1 h, see Section S.3, it can be assumed that copper oxide and cerium oxide are present as cupric oxide, CuO, and ceria, CeO_2. From the measured ICP value for Cu, see Table 1, a theoretical oxygen consumption can be calculated. Details can be found in Section S.3. The reported experimental OSC corresponds to 83.6 ± 4.7% and 80.7 ± 4.7% of the oxygen, originating from copper oxide on CuCeO and CuO respectively. From the measured ICP value for Ce, see Table 1, the reported OSC on CeO corresponds to 10.3 ± 1.5% of the oxygen, originating from ceria. When it is assumed that ceria on CuCeO is reduced to the same extend as it is the case on CeO, the obtained OSC on CuCeO matches 78.8 ± 4.5% of the oxygen, originating from cupric oxide.

Summarizing, under reduction–reoxidation conditions the copper-based catalysts provide an identical amount of oxygen, independent from the ceria present on the binary metal oxide catalyst.

3.4. Temperature-programmed desorption

From Table 2, it can be observed that the uptake of carbon dioxide on support material is higher than on impregnated material for CuCeO and CuO, indicating the absence of a significant interaction of carbon dioxide with the active phase. In contrast, CeO shows a similar carbon dioxide uptake for the support material and impregnated material. The carbon dioxide responses show three clear peaks around 350, 540 and 790 K, see Fig. 1a. For CeO the second peak is shifted toward higher temperatures. The first peak is assumed to correspond to the desorption of carbon dioxide, whereas the other two peaks can be attributed to oxygen release from the catalysts, see infra.

For the copper containing catalysts a carbon monoxide uptake is experimentally observed, whereas CeO is not able to adsorb carbon monoxide at 323 K. This is also observed by Avgouropoulos and Ioannides [34,35]. The supports show no uptake of carbon monoxide, and hence, the observed uptake is unambiguously related to the presence of copper.

Fig. 1b shows the carbon monoxide TPD response: except for CeO, the first peak around 370 K is assigned to desorption of molecular adsorbed carbon monoxide. This agrees with earlier reported carbon monoxide TPD measurements [34,35]. The other two peaks can originate from desorbing carbon dioxide, i.e., from carbon monoxide after reaction with oxygen from the metal oxide phase(s). However, when the carbon monoxide responses above 550 K are compared with the oxygen responses, see Fig. 1c, it is clear that the two peaks mainly stem from oxygen desorption.

No oxygen adsorption occurs at 323 K on the oxidized catalysts, see Section S.4, nor on the supports. In O_2-TPD performed on metal oxide catalysts, two pronounced desorption peaks are usually observed, which correspond to surface- and bulk-oxygen release respectively [36]. α-Oxygen is adsorbed on the surface oxygen vacancies and it is released at low temperature, i.e., $T_\alpha < 673$ K. The β-oxygen is observed at higher temperature, $T_\beta > 673$ K, and it corresponds to lattice oxygen. From Fig. 1c, it can be observed that the sequence of temperatures, from which oxygen is released, is: CuO (530) ≈ CuCeO (550) < CeO (630). For all tested catalysts, the second peak, corresponding to the β-oxygen, has its maximum around 790 K, although the response for CuO is somewhat flattened.

Summarizing this section, it can be concluded that carbon monoxide adsorbs selectively on cupric oxide, as reported in literature. Further, from ∼550 K on oxygen is released from the catalyst surface, indicating the oxidation capacity of the investigated metal oxide catalysts.

3.5. Structural characterization

From Fig. 2a it is observed that cupric oxide in CuCeO, as received, is identified at $2\theta = 35.5°$ and 38.7°, and ceria shows characteristic peaks at 28.6°, 47.5° and 56.3°. For CuCeO after 6000 h of experimental conditions, a shoulder for CeO_2 is observed at 47.5°, overlapping with a characteristic peak of γ-Al_2O_3 support at 45.9°. This corresponds to the observed increase in the average ceria particle size, see Table 3, going from 4.4 to 7.4 nm. Nevertheless, the long-term catalytic treatment does not affect the XRD pattern significantly, see response (1) and (5) in Fig. 2a, indicating that the catalyst is very stable when used in total oxidation environment. A possible reason is the excess of oxygen in the reaction conditions or the relative low reaction temperature, see Section 2.4, and the continuous replenishment of the oxygen vacancies preventing structural changes [37].

Fig. 2b shows XRD analysis for CuCeO as received and after a reduction treatment at 623, 923 and 1323 K, see Section 2.2. Peaks of cupric oxide at 35.5° and 38.7° disappear when reduction at 623 K is performed. Typical peaks of metallic copper appear at 43.3° and 50.4°. When reduction is performed up to 1323 K, these peaks increase in intensity. The peaks for ceria at 28.6°, 47.5° and 56.3° are invariant for the reduction up to 923 K. At the highest reduction temperature, no ceria peaks are observed, neither the partially reduced metal oxide Ce_2O_3 is observed. An aluminate, $CeAlO_3$, has been formed, which can be clearly identified at 23.6°, 33.5° and 41.4°. In a reductive atmosphere, this phase is thermodynamically favored [38]. It has to be remarked that for all applied temperatures, except the highest of 1323 K, separate phases for copper oxide and ceria are observed on the tested catalysts. The average γ-Al_2O_3 support particle size of CuCeO increases with an increasing reduction temperature, see Table 3. The average copper particle size increases with the reduction temperature up to ∼200 nm. When the half-peak width, β, is very narrow, a small experimental error corresponds to a large difference in the calculated particle size, calculated with Eq. (S-2), see Section S.5. Therefore, from particle sizes above 100 nm, accurate size determination is not possible and the copper particle size is taken in the order of

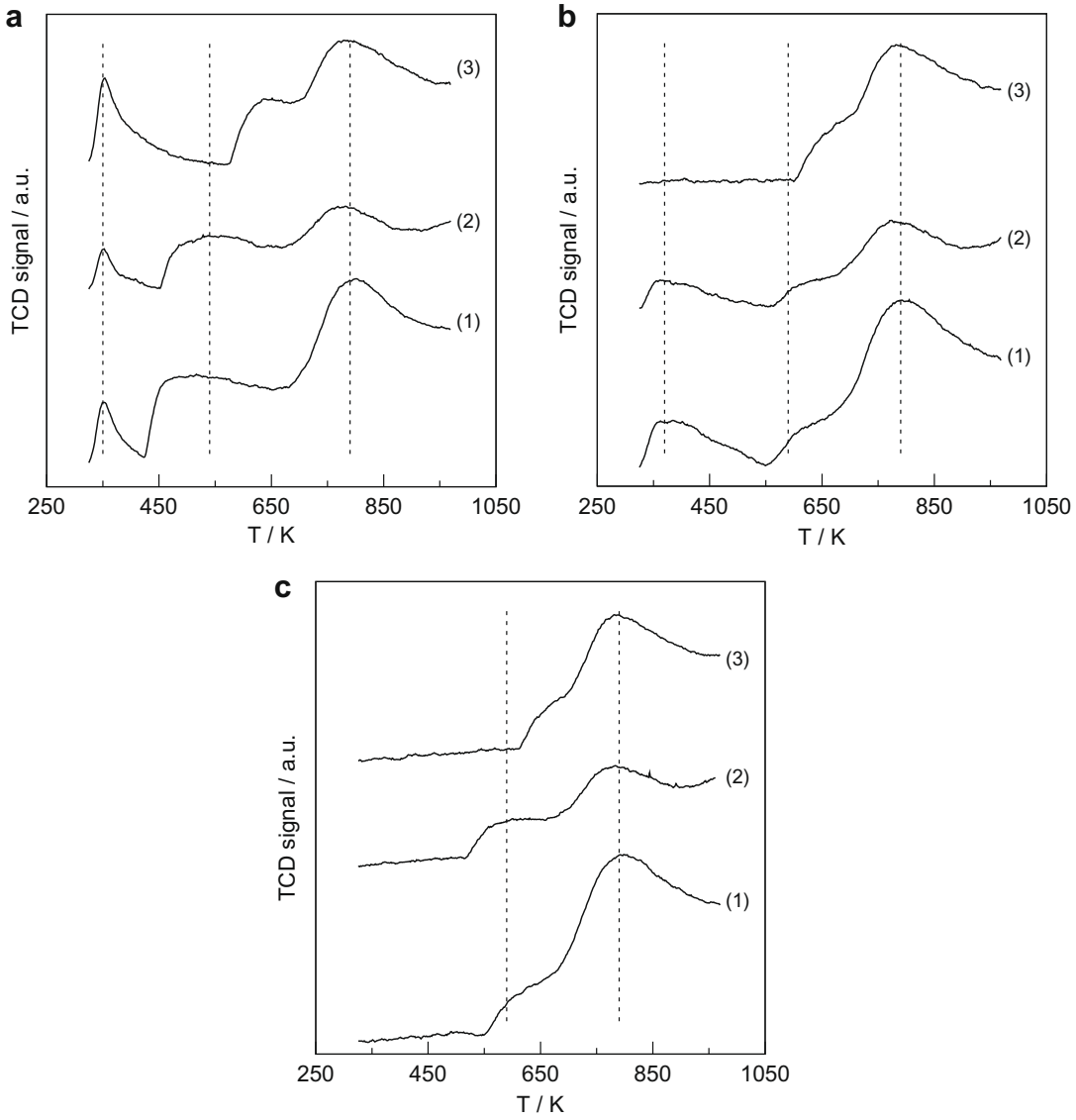

Fig. 1. Temperature-programmed desorption patterns of (a) CO_2; (b) CO; and (c) O_2. (1) CuCeO; (2) CuO; and (3) CeO.

magnitude ~100 nm. An unexpected decrease from ~100 nm to 49.1 nm is observed for the highest reduction temperature.

CuO, as received, shows cupric oxide peaks at 35.5° and 38.7° and smaller peaks at 48.7°, 58.3° and 61.5°, see Fig. 2c. The average cupric oxide particle diameter is 34.0, see Table 3. After reduction at 923 K, these peaks disappear and peaks of metallic copper are present at 43.3° and 50.4°.

Fig. 2d shows the peaks corresponding to ceria at 28.6°, 33.1°, 47.5° and 56.3°. After H_2 reduction up to 923 K, the peaks have lost some intensity, but are not significantly changed.

For CuCeO, as received, it appears that the lattice distortion parameter, ε, is higher for ceria, 15.6 mm m^{-1}, than for cupric oxide, 0.5 mm m^{-1}. This confirms the oxygen mobility of ceria under reaction conditions and, hence, the possibility of oxygen transfer, as described in literature [39]. The lattice distortion parameter for CeO, as received, and after reduction at 923 K are both 8.2 mm m^{-1}. This indicates that no structural change occurs during reduction treatment with H_2 up to the given temperature.

Summarizing this section, it can be concluded that up to 923 K only copper is reduced by H_2 and that ceria requires higher reduction temperatures. Further, the oxygen mobility for CuCeO is evidenced from the lattice distortion parameter, obtained from XRD pattern.

3.6. Temperature-programmed reduction

3.6.1. H_2-TPR

For CuCeO, three significant peaks are observed, see Fig. 3a. Two peaks occur around 430 K, which are attributed to the reduction of the cupric oxide, see Section 3.5.

From aforementioned XRD results, see Section S.5, the peak at higher temperature, shown in the inset of Fig. 3a, corresponds to the reduction of the ceria. From the estimated magnitudes, $a_{\beta^*,i}$, and standard deviations, $\sigma_{\beta^*,i}$, see Eq. (1), surface areas of the individual peaks corresponding to reduction of the cupric oxide species are calculated as $\sqrt{2\pi a_{\beta^*,i}\ \sigma_{\beta^*,i}}$. The first of two overlapping peaks covers 62.5 ± 1.1% of the total signal. Fig. 3b shows two significant peaks in the H_2-TPR spectrum for CuO. The first observed reduction peak around 450 K is about 45 K lower than the second peak temperature. The contribution of the first peak amounts to 11.6 ± 1.2%. No significant peak at higher temperature is observed on CuO, indicating that the third peak, shown in Fig. 3a, corresponds to the

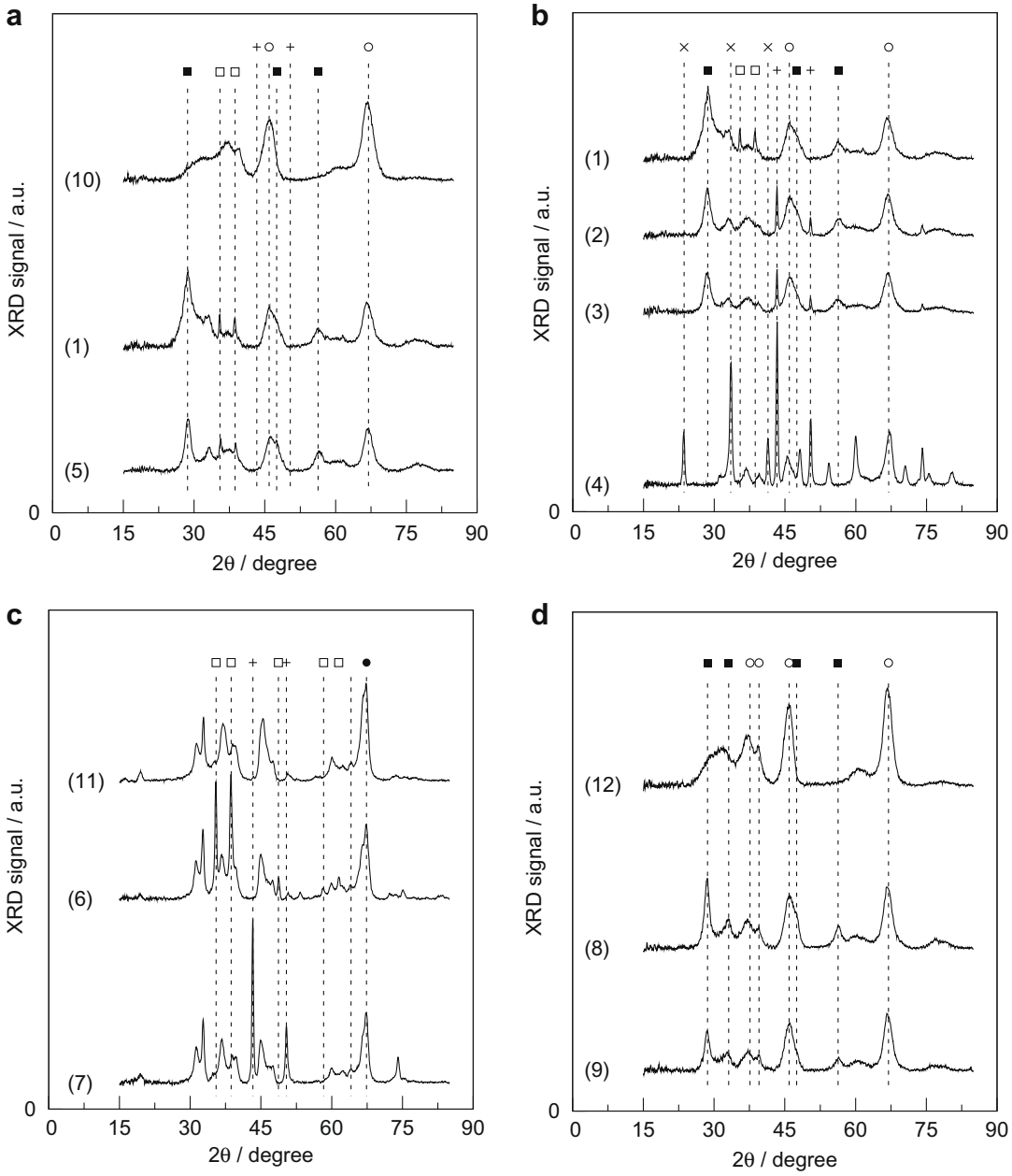

Fig. 2. XRD patterns for (a) and (b) CuCeO; (c) CuO; and (d) CeO. (□) CuO; (■) CeO_2; (+) Cu; (×) $CeAlO_3$; (○) γ-Al_2O_3; and (•) θ-Al_2O_3. The numbers between brackets correspond to the sample number as indicated in Table 3.

reduction of ceria. This is confirmed by XRD analysis of reduced catalysts up to 623 K, see Section S.5, showing no significant changes in the CeO_2 signal, see Section 3.5.

CeO shows very small peaks, when compared to the peaks corresponding to the reduction of cupric oxide, see Fig. 3c. Ceria is significantly reduced by only H_2 at temperatures higher than 623 K. It is reported that pure ceria shows two small reduction peaks at about 773 K and 1073 K, respectively [40,41]. For the other applied heating rates, see Section 2.3, the noise-to-signal ratio is too high to allow a quantitative kinetic analysis. Regressing the experimental H_2-TPR on CuCeO using three peaks in the temperature range 400–500 K, taking into account the small peak for the reduction of ceria (~440 K), did not result in significant parameter estimates. Hence, it is concluded that the presence of the small peak at lower temperatures, corresponding to a reduction of ceria, does not significantly affect the parameter estimates, corresponding to the reduction of copper oxide.

Summarizing, H_2-TPR shows two reduction peaks at lower temperatures corresponding to copper oxide reduction and only significant peaks for ceria reduction at temperatures above 623 K. The contribution of the first copper oxide reduction peak on CuCeO is five times higher compared to CuO.

3.6.2. C_3H_8-TPR

Fig. 4 shows the outlet response in C_3H_8-TPR for the tested catalysts. CuCeO shows two small peaks at 404 and 446 K. Two pronounced overlapping peaks are observed at 597 and 674 K. In the latter peak, a shoulder around 728 K is present. CuO has also two small peaks at 439 and 510 K. These peaks clearly correspond to the small peaks on CuCeO, but they are shifted by 35 K. Further, two pronounced and also overlapping peaks are observed at 653 and 711 K.

CeO shows three small peaks at 481, 612 and 782 K. The shoulder around 728 K for CuCeO does not occur on CuO. Hence, this can

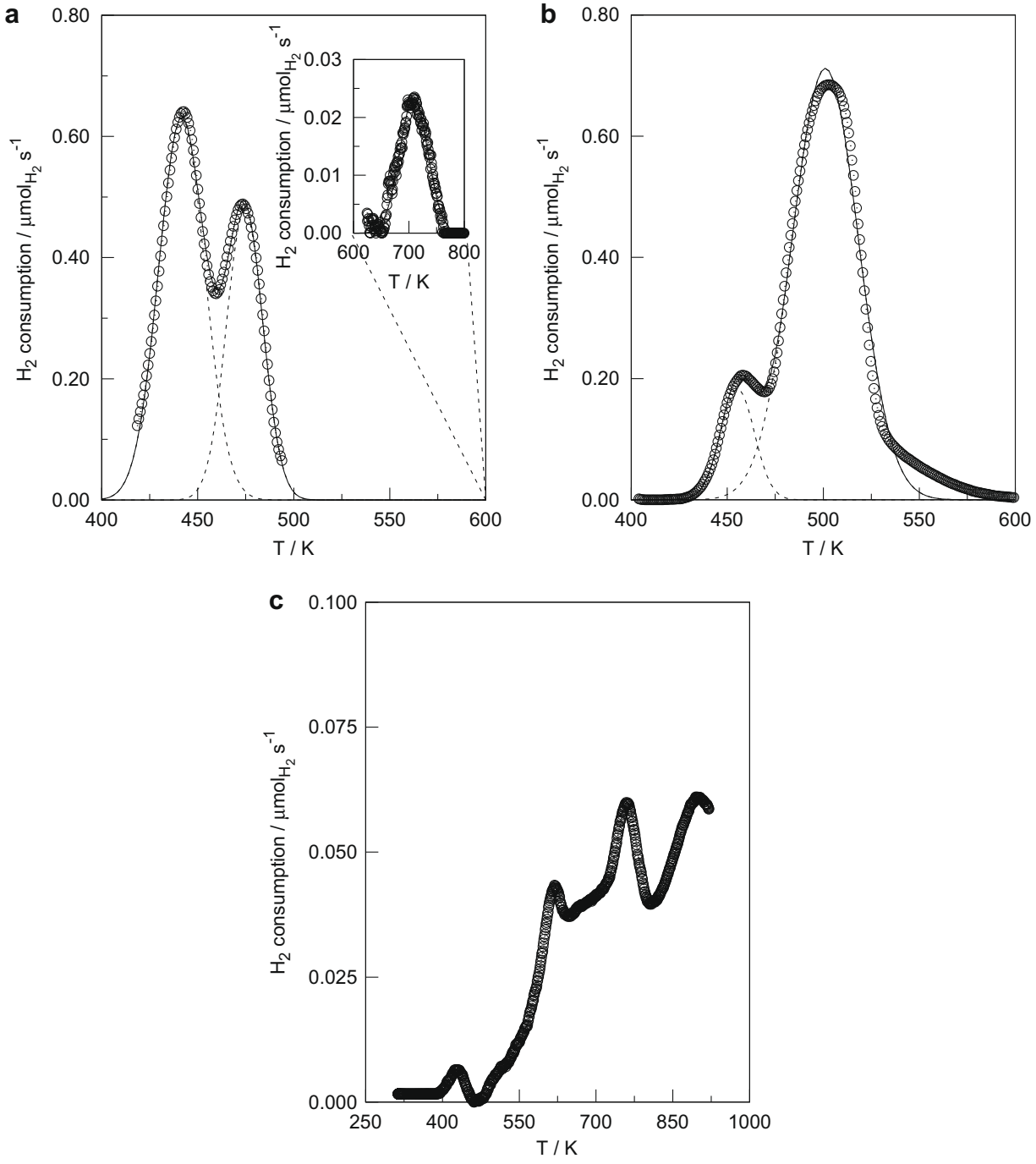

Fig. 3. H_2 consumption versus temperature at a heating rate of 10.0 K min^{-1} in H_2-TPR. (a) CuCeO; (b) CuO; and (c) CeO. (○) experimental measurement (—) calculated TCD response, using Eq. (1); (- - -) deconvoluted peaks.

be attributed to interaction between cupric oxide and ceria. Due to this interaction, the peak at 782 K on CeO is probably shifted to 728 K on CuCeO, corresponding to an easier reduction.

Summarizing, it is observed in C_3H_8-TPR that reduction peaks shift toward lower temperatures when cupric oxide and ceria are present together.

3.7. Concentration of active sites

There are three possible ways to quantify the total active site concentration: (i) TPD of carbon monoxide, (ii) TPR with H_2 and (iii) reduction/reoxidation pulse experiments at a given temperature, i.e., the OSC. Carbon monoxide TPD experiments allow a quantification of the surface cupric oxide species only. Although the amount of hydrogen consumed in a TPR experiment can in principle be used as a measure of the total active site concentration [42], the TPR spectra obtained on CeO only allow a qualitative interpretation in terms of reducibility rather than a quantification of the total concentration of active sites, see Section 3.6.1. Therefore, the OSC is used as a measure for the total concentration of active sites. It is reported that for ceria-based catalysts, only the surface oxygen is addressed [43]. However, in the present work, the OSC is used. Although this value is not limited to oxygen present at the catalyst surface but also accounts for some sub-surface oxygen, i.e., the value is one order of magnitude larger, it is expected to provide a sound basis for comparison assuming that

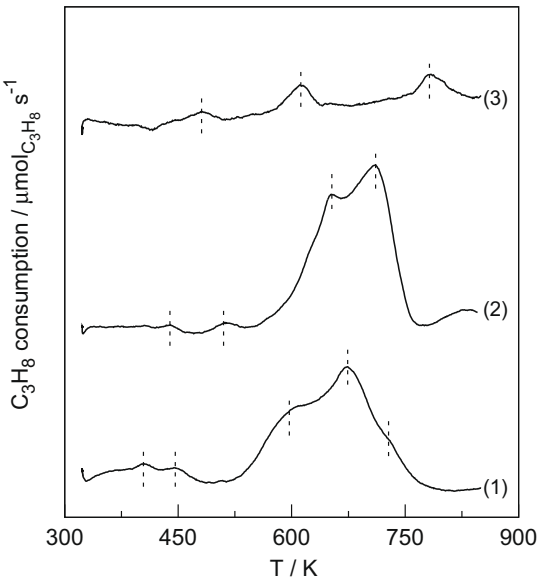

Fig. 4. Outlet response versus temperature at a heating rate $\beta = 10.0\ \mathrm{K\ min^{-1}}$ in C_3H_8-TPR. (1) CuCeO; (2) CuO; and (3) CeO. Maxima are indicated per catalyst by dashed lines.

the OSC is at least proportional if not representative for the amount of oxygen that can participate in the reaction [19].

In this work, the OSC is determined at 673 K, i.e., 25 K above the highest temperature used in the experimental program, see Section 3.3.

4. Kinetics

4.1. H_2-TPR

Linear regression of the experimental data, $(T_{\beta^*,i}, \beta_i^*)$, with Eq. (3), results in the estimation of the preexponential factor A_i and the activation energy E_i, corresponding to the ith peak in the TPR response. The parameter estimates and their 95% confidence intervals are listed in Table 4. A maximum binary correlation coefficient of 0.88 is obtained, meaning that there is no significant correlation between the two corresponding parameters.

It is observed that the activation energy for the H_2 reduction corresponding to the first peak is higher than the value for the second peak. The corresponding preexponential factors compensate for this phenomenon, as also observed by Besselmann et al. [44] in their TPR experiments using V_2O_5/TiO_2 catalysts: although monomeric vanadyl species are more easily reduced than polymeric species, i.e., at a lower temperature, the reduction of the former requires a higher activation energy than the latter.

4.2. Steady-state total oxidation

4.2.1. TOF_0 analysis

Fig. 5a depicts the experimental propane conversion versus space time for the tested catalysts. Experimental propane conversion versus temperature for the total oxidation of propane is presented in Fig. 5b. For CuO, duplicated experiments are reported.

Experimental apparent activation energies, E_{app}^{obs}, for the total oxidation of propane, obtained via Eq. (7), are reported in Table 5. The experimental apparent activation energy for CuCeO is

Table 4
Parameter estimates with their 95% confidence intervals from regression of H_2-TPR data with Eq. (3) for CuCeO and CuO.

Catalyst	A_1 (s^{-1})	E_1 (kJ mol−1)	A_2 (s^{-1})	E_2 (kJ mol^{-1})	A_3 (s^{-1})	E_3 (kJ mol^{-1})
CuCeO	$(6.71 \pm 1.47) \times 10^{+6}$	81.3 ± 4.2	$(1.43 \pm 0.22) \times 10^{+4}$	62.6 ± 3.1	$(9.33 \pm 4.11) \times 10^{+8}$	151.2 ± 12.7
CuO	$(3.72 \pm 1.18) \times 10^{+5}$	67.8 ± 5.8	$(2.69 \pm 1.21) \times 10^{+4}$	64.9 ± 8.9		

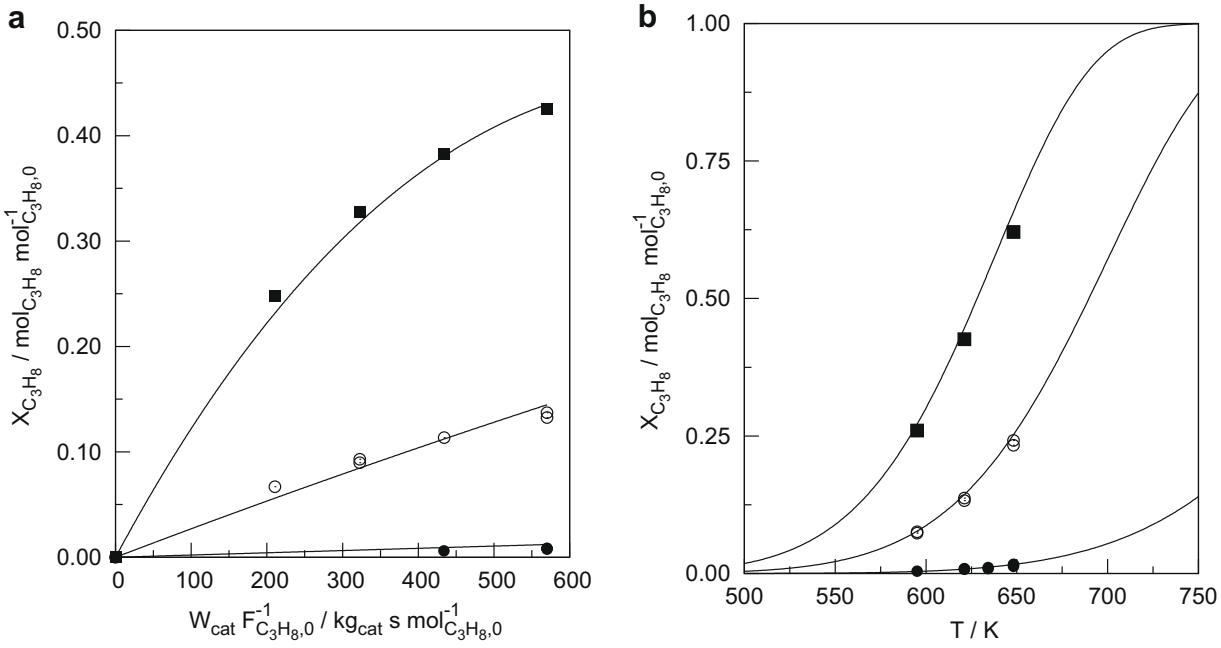

Fig. 5. (a) Propane conversion versus space time at $T = 621$ K. (b) Propane conversion versus temperature at $W_{cat}F^{-1}_{C_3H_8,0} = 570\ kg_{cat}\ s\ mol^{-1}_{C_3H_8,0}$. $p_{C_3H_8,0} = 0.6$ kPa and $p_{O_2,0} = 3.5$ kPa. (■) CuCeO; (○) CuO; and (●) CeO. Full lines are obtained with the MVK model, see Eq. (9), and corresponding parameter estimates from Table 6.

Table 5
Initial steady-state reaction kinetic parameter estimates with their 95% confidence intervals, according to Eqs. (7) and (8). Temperature range: 595–648 K.

Catalyst	TOF_0 at 621 K ($mol_{C_3H_8}\ mol_O^{-1}\ s^{-1}$)	$k^*_{app,0}$ ($mol_{C_3H_8}\ mol_O^{-1}\ s^{-1}$)	E^{obs}_{app} (kJ mol^{-1})
CuCeO	$(1.46 \pm 0.14) \times 10^{-3}$	$(1.25 \pm 0.50) \times 10^{2}$	59.7 ± 8.2
CuO	$(2.72 \pm 0.32) \times 10^{-4}$	$(2.20 \pm 0.20) \times 10^{3}$	81.4 ± 3.5
CeO	$(2.10 \pm 0.11) \times 10^{-4}$	$(1.72 \pm 0.18) \times 10^{3}$	82.1 ± 4.1

~20 kJ mol^{-1} lower than that for CuO and CeO. The TOF_0 follows the order CuCeO > CuO > CeO.

4.2.2. Mars–van Krevelen (MVK) parameter estimates

The parameter estimates with their 95% confidence intervals, obtained by regression of the experimental data with the MVK model, see Eq. (9), are listed in Table 6. The calculated F value for each of the tested catalysts by far exceeds the tabulated value, F_{tab} = 3.98, and hence, the global regression is significant. A good agreement between experimental and calculated data is obtained, see Fig. 5a and b.

The average fraction of oxidized sites for the tested catalysts during reaction conditions, $\bar{\theta}_{O^*}$, obtained with Eq. (13), is listed in Table 6. At the investigated reaction conditions, ~45% of the active sites are oxidized for CuCeO. A fraction of oxidized sites of ~100% is obtained for CuO, and hence, the observed apparent activation energy equals the activation energy for reduction, see Eq. (12). For CeO, the average fraction of oxidized sites is not significantly different from zero, and hence, the apparent activation energy is assumed to correspond to the activation energy for reoxidation under the given reaction conditions.

The estimates for the activation energies in the total oxidation of propane, determined by TOF_0 analysis, see Table 5, are satisfactorily within the range of 70–110 kJ mol^{-1}. For the proposed MVK model, see Eq. (9), the activation energies for the reduction are also within the proposed range, whereas values for the reoxidation display somewhat lower, but still acceptable values.

Standard activation entropies for oxygen and propane adsorption are given in Table 7. Gas phase entropy values for oxygen and propane, calculated at T = 621 K, are 226 and 270 J mol^{-1} K^{-1} [31], and hence, physically relevant values are obtained with Eq. (14). The values calculated for the standard activation entropies are reasonably within the proposed range of −130 to −210 J mol^{-1} K^{-1}, see Section 2.4.4. Oxygen and propane standard activation entropies for CuCeO and CuO are similar. CeO has oxygen activation entropy of ~20 J mol^{-1} K^{-1} less than obtained for CuCeO, whereas the propane adsorption is ~40 J mol^{-1} K^{-1} lower.

5. Discussion

The H_2-TPR data could be interpreted as the consequence of a consecutive reduction mechanism of the cupric oxide over cuprous oxide to metallic copper species under the given experimental reduction conditions [45], see Eqs. (16) and (17):

$$2CuO + H_2 \rightarrow Cu_2O + H_2O \quad (16)$$

$$Cu_2O + H_2 \rightarrow Cu + H_2O \quad (17)$$

In this case, the second reduction step requires a double amount of H_2, compared to the first reduction step. This is not consistent with the calculated ratio of H_2-TPR peak surface areas for CuCeO and CuO, 62.5 ± 1.1% and 11.6 ± 1.2% respectively, see Section 3.6.1.

An alternative interpretation for the occurrence of the first of the two reduction peaks could be the presence of finely dispersed cupric oxide particles: it is reported that for a low copper content only one peak arises, but from about 5–7 wt.% on two peaks are present in the corresponding H_2-TPR response [46]. The copper loading of the tested samples is above this threshold value, see Table 1, and therefore, the peak at lower temperature could be attributed to the reduction of dispersed copper species and the second peak to the reduction of larger copper oxide particles [47,48]. However, XRD analysis does not significantly reveal any of these finely dispersed species [49]. Therefore, it is proposed that the first reduction peak corresponds to the reduction of the outer surface of the cupric oxide particle and the reduction of the bulk of the cupric oxide particle, more difficult to realize, of rise to a second peak. Concerning the first reduction, no specific copper oxide planes, e.g., (1 1 1) and (1 0 0) [50], are taken into account, i.e., average surface properties are considered. According to Silversmit et al. [51], the reduction of ceria occurs in a similar way. It is noteworthy to mention that the reduction mechanism of the cupric oxide particles, see Eqs. (16) and (17), cannot be excluded; the outer surface and the bulk of the particles can be reduced in a two-step mechanism, but the present data cannot distinguish between them.

Table 6
Parameter estimates with their 95% confidence intervals, obtained by non-isothermal regression of the experimental data with the proposed MVK model, given by Eq. (9), for the tested catalysts. The average fraction of oxidized sites, $\bar{\theta}_{O^*}$, is obtained with Eq. (13), and corresponding standard deviations are calculated from the 95% confidence intervals for the activation energies E_{O_2}, $E_{C_3H_8}$ and E^{obs}_{app} given in Table 5. F_{tab} = 3.98.

Catalyst	F_{calc} (mol^2 mol^{-2})	$k_{O_2,0}$ ($mol_{C_3H_8}\ mol_O^{-1}\ s^{-1}\ kPa^{-1}$)	E_{O_2} (kJ mol^{-1})	$k_{C_3H_8,0}$ ($mol_{C_3H_8}\ mol_O^{-1}\ s^{-1}\ kPa^{-1}$)	$E_{C_3H_8}$ (kJ mol^{-1})	$\bar{\theta}_{O^*}$ (–)
CuCeO	467	$(2.01 \pm 0.65) \times 10^{-1}$	47.2 ± 3.5	$(3.29 \pm 1.07) \times 10^{0}$	74.9 ± 5.5	0.45 ± 0.06
CuO	873	$(2.46 \pm 0.72) \times 10^{-1}$	50.8 ± 2.4	$(1.39 \pm 0.41) \times 10^{0}$	78.5 ± 3.7	1.11 ± 0.20
CeO	435	$(2.11 \pm 0.62) \times 10^{+0}$	77.9 ± 4.4	$(2.97 \pm 0.87) \times 10^{2}$	102.5 ± 5.9	0.17 ± 0.23

Table 7
Standard activation entropies calculated from Eq. (14), along with their standard deviations obtained from error propagation. The considered errors are those on the estimated value of the rate coefficient (see Table 6) and the experimentally measure oxygen storage capacity (see Table 2). Sticking probability s for oxygen and propane with their standard deviations obtained from error propagation. The considered errors are those on the estimated value of the rate coefficient (see Table 6).

Catalyst	$\Delta^{\neq}S^{0a}$ (J mol^{-1} K^{-1})		Sticking probability s^a (–)	
	O_2	C_3H_8	O_2	C_3H_8
CuCeO	−213.1 ± 5.4	−204.9 ± 5.7	$(9.57 \pm 3.07) \times 10^{-3}$	$(2.67 \pm 0.86) \times 10^{-4}$
CuO	−211.4 ± 4.9	−212.1 ± 5.2	$(1.09 \pm 0.32) \times 10^{-3}$	$(3.05 \pm 0.88) \times 10^{-5}$
CeO	−193.8 ± 4.9	−167.7 ± 5.2	$(7.52 \pm 2.17) \times 10^{-3}$	$(2.10 \pm 0.61) \times 10^{-6}$

[a] T = 621 K.

From the estimated activation energies and preexponential factors for H_2 reduction, reported in Table 4, it can be concluded that impregnation with $Ce(NO_3)_4$ does not significantly affect the reduction characteristics for the second peak of CuCeO, when compared to CuO. This agrees with the proposition that the second peak in the H_2-TPR reduction corresponds to the reduction of the bulk part of the cupric oxide particles, i.e., independent of the ceria. Further, from the ratio in surface areas for the first reduction peak obtained on CuCeO and CuO, 62.5 ± 1.1% and 11.6 ± 1.2% respectively, it can be concluded that addition of ceria enhances the reduction, and hence, it improves the total oxidation activity, as evidenced from Figs. 4–6. The electronic interaction between Ce 4f, O 2p and Cu 3d orbitals and the corresponding higher oxidation activity are described by Bera et al. [52]. These interactions are believed to be responsible for the superior activity of the CuO–CeO_2 catalyst, compared to a CuO or CeO_2 catalyst [34,35].

The lattice distortion parameter, obtained in Section 3.5, is an indication for the higher propane conversion and corresponding TOF on the latter catalyst. This is consistent with the obtained C_3H_8-TPR reduction characteristics, see Section 3.6.2.

From the obtained average fraction of oxidized sites, $\bar{\theta}_{O^*}$, see Table 6, it can be put forward that the reduction step is the most critical step in the reaction mechanism of propane total oxidation on CuO, whereas it is the reoxidation that is critical on CeO, see Section 4.2.2. The binary metal oxide, CuCeO, allows a combination of the good characteristics of both types of oxides in a synergistic way. Using the parameter estimates, given in Table 6, and the oxygen concentration C_O, given in Table 2, the TOF_0 is calculated for CuCeO, CuO and CeO according to the proposed MVK model, see Eq. (9). At the present experimental conditions, it is observed from Fig. 6 that CuO shows a slightly higher TOF_0 than CeO, especially for higher temperatures. The ratio of the TOF_0 obtained on CuCeO to the sum of the TOF_0 calculated for CuO and CeO is plotted on the right vertical axis.

Using the OSC values, see Table 2, and the TOF_0 at 621 K for the used catalysts, see Table 5, synergistic effect occurs for the binary metal oxide catalyst when the TOF_0 is higher than 2.60× 10^{-4} $mol_{C_3H_8}$ mol_O^{-1} s^{-1}. The TOF_0 at 621 K on CuCeO is 1.46× 10^{-3} $mol_{C_3H_8}$ mol_O^{-1} s^{-1}, and hence, a synergistic effect is observed. Moreover, at each temperature level, see Fig. 6, the TOF_0 for CuCeO is even higher than the sum of TOF_0 for CuO and CeO: the ratio of TOF_0 varies from 5.9, at lower reaction temperature, to 1.9 at higher reaction temperatures. This confirms the synergy for all the applied experimental conditions in the case of the binary metal oxide catalyst and the given compromise between reoxidation and reduction properties, obtained from the calculated average fraction of oxidized sites, $\bar{\theta}_{O^*}$, see Table 6. Using binary metal oxide catalysts, based on CuO and CeO_2, synergy is observed in various oxidation studies [33,48,53–56].

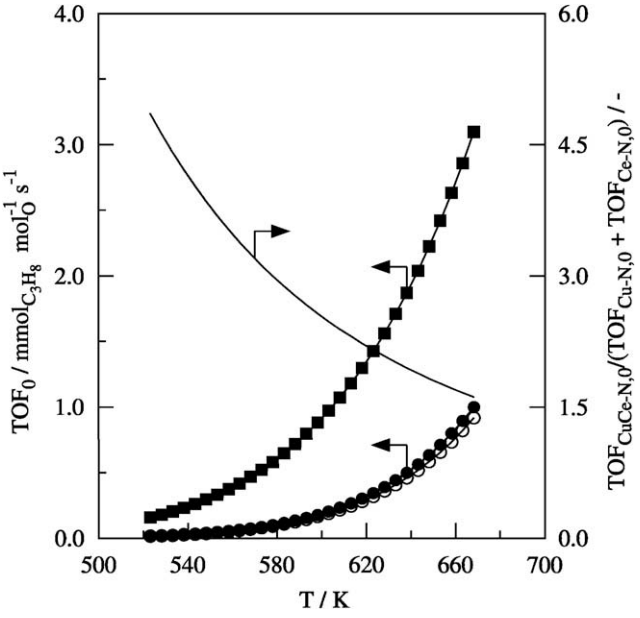

Fig. 6. TOF_0 versus temperature. $p_{C_3H_8,0}$ = 0.6 kPa and $p_{O_2,0}$ = 3.5 kPa. (■) CuCeO; (○) CuO; and (●) CeO. Points and full lines are obtained with the MVK model, see Eq. (9), and corresponding parameter estimates from Table 6. The right axis gives the ratio of the calculated TOF_0 for CuCeO to the sum of the calculated TOF_0, obtained on CuO and CeO.

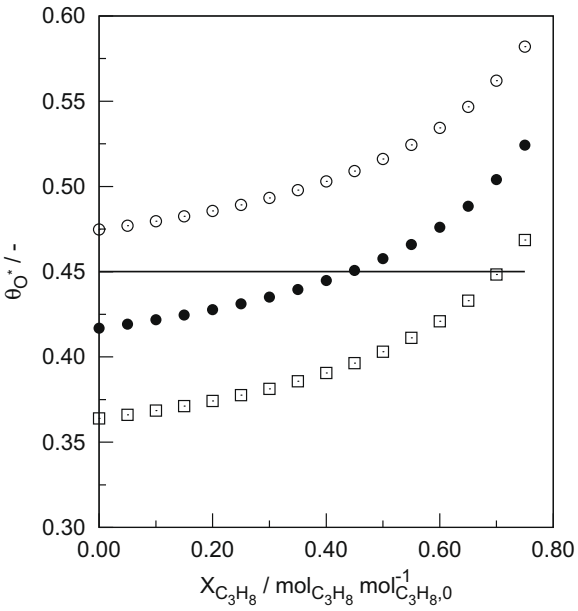

Fig. 7. Fraction of oxidized sites on CuCeO versus propane conversion. The former is calculated with Eq. (10), using Eqs. (S-18) and (S-19) and the corresponding parameter estimates from Table 6. $p_{C_3H_8,0}$ = 0.6 kPa and $p_{O_2,0}$ = 3.5 kPa. (□) 595 K; (●) 621 K; and (○) 648 K. The full line indicates the average fraction of oxidized sites, $\bar{\theta}_{O^*}$, obtained with Eq. (13), see Appendix A.

Often, the reaction temperature, $T_{0.50}$, for which the propane conversion is 0.50 $mol_{C_3H_8}$ $mol_{C_3H_8,0}^{-1}$, is taken as a measure for catalytic activity [57] The following ranking is consistent with the TOF_0: CuCeO ($T_{0.50}$ = 628 K) > CuO (690) > CeO (842), see Fig. 5b.

The sticking probabilities s for oxygen and propane are given in Table 7. For CuCeO, the value for propane is an order of magnitude lower, compared to oxygen. Sticking probabilities for propane and oxygen on CuO are about one order of magnitude lower than for CuCeO. Overall two order of magnitudes lower, compared to CuCeO, sticking probabilities for oxygen and propane are obtained for CeO. The values for the sticking probability, together with the above given arguments, can be an explanation for the superior activity of CuCeO, compared to CuO and CeO.

6. Conclusions

Turnover frequencies are highest on the binary metal oxide catalyst, CuO–CeO_2/γ-Al_2O_3: the reduction and reoxidation characteristics of both types of single metal oxides are combined in a synergistic way. The average fractions of oxidized and reduced sites are close to 0.5 over the investigated range of experimental conditions. This suggests that the formulation of the binary oxide catalyst used is close to optimum. It is proposed that the reduction of cupric oxide particles on the catalysts used in this paper occurs

via a first reduction of the outer surface of the particles, followed by a subsequent reduction of the bulk.

Acknowledgments

This work was performed in the framework of a Concerted Research Action (GOA), financed by Ghent University. The project 1.5.201.07 sponsored by the FWO-Vlaanderen is also gratefully acknowledged. This work has also partly been performed within the IAP-PAI framework sponsored by the Belgian Science Policy.

Appendix A. Mathematical derivation of Eq. (12)

For a reaction rate coefficient, k_i, the Arrhenius temperature dependency is given by Eq. (18):

$$k_i = k_{i,0} \exp\left(-\frac{E_i}{RT}\right) \tag{18}$$

Application of Eq. (11) to Eq. (9), using identity (19) and Eq. (20), gives Eq. (21). Introduction of Eq. (10) into Eq. (21) gives Eq. (12).

$$\frac{\partial}{\partial T} \ln \frac{1}{f(T)} = -\frac{1}{f(T)} \frac{\partial f(T)}{\partial T} \tag{19}$$

$$\frac{\partial k_i}{\partial T} = k_i \frac{E_i}{RT^2} \tag{20}$$

$$E_{\text{app}}^{\text{calc}} = \frac{5k_{C_3H_8} p_{C_3H_8}}{k_{O_2} p_{O_2} + 5k_{C_3H_8} p_{C_3H_8}} E_{O_2} + \frac{k_{O_2} p_{O_2}}{k_{O_2} p_{O_2} + 5k_{C_3H_8} p_{C_3H_8}} E_{C_3H_8} \tag{21}$$

Fig. 7 gives the fraction of oxidized sites, calculated with Eq. (10), versus the propane conversion at $p_{C_3H_8,0} = 0.6$ kPa, $p_{O_2,0} = 3.5$ kPa and different temperatures. Zero propane conversion mimics the inlet of the reactor bed. The experimental propane conversion mounts to 0.73 $\text{mol}_{C_3H_8}\ \text{mol}_{C_3H_8,0}^{-1}$, see Section 2.4, which corresponds to the outlet of the reactor bed. The average value of the fraction of oxidized sites, given in Eq. (13), is 0.45 ± 0.06.

Appendix B. Supplementary material

Supplementary data associated with this article can be found in the online version at doi:10.1016/j.jcat.2010.03.006.

References

[1] E.C. Moretti, Practical Solutions for Reducing Volatile Organic Compounds and Hazardous Air Pollutants, AIChE CWRT, New York, 2001. 150 pp.
[2] M. Zimowska, A. Michalik-Zym, R. Janik, T. Machej, J. Gurgul, R.P. Socha, J. Podobinski, E.M. Serwicka, Catal. Today 119 (2007) 321–326.
[3] G. Busca, E. Finocchio, G. Ramis, G. Ricchiardi, Catal. Today 32 (1996) 133–143.
[4] E.M. Cordi, P.J. O'Neill, J.L. Falconer, Appl. Catal., B: Environ. 14 (1997) 23–36.
[5] G.J. Hutchings, S.H. Taylor, Catal. Today 49 (1999) 105–113.
[6] V.C. Belessi, A.K. Ladavos, G.S. Armatas, P.J. Pomonis, Phys. Chem. Chem. Phys. 3 (2001) 3856–3862.
[7] V.C. Belessi, A.K. Ladavos, P.J. Pomonis, Appl. Catal., B: Environ. 31 (2001) 183–194.
[8] P. Djinovic, J. Batista, A. Pintar, Appl. Catal., A: Gen. 347 (2008) 23–33.
[9] P. Djinovic, J. Levec, A. Pintar, Catal. Today 138 (2008) 222–227.
[10] G. Ertl, H. Knözinger, J. Weitkamp, Preparation of Solid Catalysts, Wiley-VCH, Weinheim, 1999. 622 p.
[11] J.A. Schwarz, C. Contescu, A. Contescu, Chem. Rev. 95 (1995) 477–510.
[12] S. Brunauer, P.H. Emmett, E. Teller, J. Am. Chem. Soc. 60 (1938) 309–319.
[13] R. Radhakrishnan, S.T. Oyama, J. Catal. 204 (2001) 516–519.
[14] P. Scherrer, Nachr. Ges. Wiss. Göttingen, Math. – Phys. Kl 2 (1918) 98–100.
[15] G.K. Williamson, W.H. Hall, Acta Metall. 1 (1953) 22–31.
[16] P.M. Heynderickx, J.W. Thybaut, H. Poelman, D. Poelman, G.B. Marin, Appl. Catal., B: Environ. 95 (2010) 26–38.
[17] S.J. Gentry, N.W. Hurst, A. Jones, J. Chem. Soc., Faraday Trans. 75 (1979) 1688–1699.
[18] G. Ertl, H. Knözinger, J. Weitkamp, Handbook of Heterogeneous Catalysis, Wiley-VCH, Weinheim, 1997. 2479 p.
[19] P.M. Heynderickx, J.W. Thybaut, H. Poelman, D. Poelman, G.B. Marin, Appl. Catal., B: Environ. 90 (2009) 295–306.
[20] R.J. Berger, E.H. Stitt, G.B. Marin, F. Kapteijn, J.A. Moulijn, Cattech 5 (2001) 30–60.
[21] G. Arzamendi, V.A.D. O'Shea, M.C. Alvarez-Galvan, J.L.G. Fierro, P.L. Arias, L.M. Gandia, J. Catal. 261 (2009) 50–59.
[22] J.L. Ayastuy, A. Gurbani, M.P. Gonzalez-Marcos, M.A. Gutierrez-Ortiz, Ind. Eng. Chem. Res. 48 (2009) 5633–5641.
[23] V.R. Choudhary, G.M. Deshmukh, Chem. Eng. Sci. 60 (2005) 1575–1581.
[24] T.K. Tseng, H. Chu, T.H. Ko, L.K. Chaung, Chemosphere 61 (2005) 469–477.
[25] C.H. Wang, S.S. Lin, H.S. Weng, J. Environ. Sci. Health., Part A: Toxic/Hazard. Subst. Environ. Eng. 37 (2002) 1649–1663.
[26] M.A. Vannice, Kinetics of Catalytic Reactions, Springer, New York, 2005. 240 p.
[27] I. Chorkendorff, J.W. Niemantsverdriet, Concepts of Modern Catalysis and Kinetics, Wiley-VCH, Weinheim, 2007. 457 p.
[28] J.I. Steinfeld, J.S. Francisco, W.L. Hase, Chemical Kinetics and Dynamics, Prentice Hall, Upper Saddle River, NJ, 1999. 518 p.
[29] G.C. Bond, M.A. Keane, H. Kral, J.A. Lercher, Catal. Rev. – Sci. Eng. 42 (2000) 323–383.
[30] G. Fu, X. Xu, X. Lu, H. Wan, J. Phys. Chem. B 109 (2005) 6416–6421.
[31] http://cccbdb.nist.gov.
[32] M. Baldi, E. Finocchio, F. Milella, G. Busca, Appl. Catal., B: Environ. 16 (1998) 43–51.
[33] N.R.E. Radwan, G.A. Fagal, G.A. El-Shobaky, Colloids Surf., A 178 (2001) 277–286.
[34] G. Avgouropoulos, T. Ioannides, Catal. Lett. 116 (2007) 15–22.
[35] G. Avgouropoulos, T. Ioannides, J. Mol. Catal. A: Chem. 296 (2008) 47–53.
[36] R. Pereniguez, J.L. Hueso, J.P. Holgado, F. Gaillard, A. Caballero, Catal. Lett. 131 (2009) 164–169.
[37] U. Lassi, R. Polvinen, S. Suhonen, K. Kallinen, A. Savimaki, M. Harkonen, M. Valden, R.L. Keiski, Appl. Catal., A: Gen. 263 (2004) 241–248.
[38] D.E. Angove, N.W. Cant, D.H. French, K. Kinealy, Appl. Catal., A: Gen. 194 (2000) 27–34.
[39] T.G. Kuznetsova, V.A. Sadykov, Kinet. Catal. 49 (2008) 840–858.
[40] M. Boaro, M. Vicario, C. de Leitenburg, G. Dolcetti, A. Trovarelli, Catal. Today 77 (2003) 407–417.
[41] T. Caputo, L. Lisi, R. Pirone, G. Russo, Appl. Catal., A: Gen. 348 (2008) 42–53.
[42] B. Moden, L. Oliviero, J. Dakka, J.G. Santiesteban, E. Iglesia, J. Phys. Chem. B 108 (2004) 5552–5563.
[43] S. Bedrane, C. Descorme, D. Duprez, Catal. Today 75 (2002) 401–405.
[44] S. Besselmann, C. Freitag, O. Hinrichsen, M. Muhler, Phys. Chem. Chem. Phys. 3 (2001) 4633–4638.
[45] X.Q. Wang, J.C. Hanson, A.I. Frenkel, J.Y. Kim, J.A. Rodriguez, J. Phys. Chem. B 108 (2004) 13667–13673.
[46] L. Kundakovic, M. Flytzani-Stephanopoulos, Appl. Catal., A: Gen. 171 (1998) 13–29.
[47] J. Beckers, G. Rothenberg, Dalton Trans. 46 (2008) 6573–6578.
[48] W. Liu, M. Flytzani-Stephanopoulos, J. Catal. 153 (1995) 304–316.
[49] J.W. Niemantsverdriet, Spectroscopy in Catalysis: An Introduction, Wiley-VCH, Weinheim, 2007. 325 p.
[50] R.W.G. Wyckoff, Crystal Structures, Interscience Publishers, New York, 1963.
[51] G. Silversmit, H. Poelman, V. Balcaen, P.M. Heynderickx, M. Olea, S. Nikitenko, W. Bras, P.F. Smet, D. Poelman, R. De Gryse, M.-F. Reniers, G.B. Marin, J. Phys. Chem. Solids 70 (2009) 1274–1284.
[52] P. Bera, S. Mitra, S. Sampath, M.S. Hegde, Chem. Commun. (2001) 927–928.
[53] W. Liu, M. Flytzani-Stephanopoulos, J. Catal. 153 (1995) 317–332.
[54] W. Liu, A.F. Sarofim, M. Flytzani-Stephanopoulos, Chem. Eng. Sci. 49 (1994) 4871–4888.
[55] A. Martinez-Arias, M. Fernandez-Garcia, J. Soria, J.C. Conesa, J. Catal. 182 (1999) 367–377.
[56] A. Martinez-Arias, A.B. Hungria, G. Munuera, D. Gamarra, Appl. Catal., B: Environ. 65 (2006) 207–216.
[57] V. Blasin-Aubé, J. Belkouch, L. Monceaux, Appl. Catal., B: Environ. 43 (2003) 175–186.